Storm-Relative Helicity Revealed from Polarimetric Radar Measurements

MATTHEW R. KUMJIAN AND ALEXANDER V. RYZHKOV

Cooperative Institute for Mesoscale Meteorological Studies, University of Oklahoma, and NOAA/OAR/National Severe Storms Laboratory, Norman, Oklahoma

(Manuscript received 14 April 2008, in final form 27 August 2008)

ABSTRACT

The dual-polarization radar variables are especially sensitive to the microphysical processes of melting and size sorting of precipitation particles. In deep convective storms, polarimetric measurements of such processes can provide information about the airflow in and around the storm that may be used to elucidate storm behavior and evolution. Size sorting mechanisms include differential sedimentation, vertical transport, strong rotation, and wind shear. In particular, winds that veer with increasing height typical of supercell environments cause size sorting that is manifested as an enhancement of differential reflectivity (Z_{DR}) along the right or inflow edge of the forward-flank downdraft precipitation echo, which has been called the Z_{DR} arc signature. In some cases, this shear profile can be augmented by the storm inflow. It is argued that the magnitude of this enhancement is related to the low-level storm-relative environmental helicity (SRH) in the storm inflow.

To test this hypothesis, a simple numerical model is constructed that calculates trajectories for raindrops based on their individual sizes, which allows size sorting to occur. The modeling results indicate a strong positive correlation between the maximum Z_{DR} in the arc signature and the low-level SRH, regardless of the initial drop size distribution aloft. Additional observational evidence in support of the conceptual model is presented. Potential changes in the Z_{DR} arc signature as the supercell evolves and the low-level mesocyclone occludes are described.

1. Introduction

a. Polarimetric variables

Dual-polarization radar observations provide insight into microphysical processes in clouds and precipitation. By receiving signals at orthogonal polarizations, information is gathered about bulk particle properties within the sampling volume, such as size, shape, composition, and diversity (e.g., Herzegh and Jameson 1992; Zrnić and Ryzhkov 1999; Bringi and Chandrasekar 2001). The simultaneous transmission of horizontally and vertically polarized radio waves allows for several polarimetric variables to be estimated, including the differential reflectivity (Z_{DR}), differential phase shift (Φ_{DP}), and copolar cross-correlation coefficient (ρ_{HV}). These quantities supplement the conventional radar signals of the reflectivity factor at horizontal polarization (Z_{HH}) and Doppler velocity (v_r). The logarithmic ratio between backscattered power returned to the radar at horizontal polarization and vertical polarization, Z_{DR} (Seliga and Bringi 1976), is sensitive to the shape, orientation, density, and phase composition of hydrometeors in the sampling volume, but not to their concentration. Because raindrop oblateness increases with diameter (Pruppacher and Pitter 1971), Z_{DR} increases with increasing raindrop size. Hydrometeors with isotropic scattering characteristics (e.g., spherical particles or chaotically tumbling particles) have an intrinsic Z_{DR} of 0 dB. For a given shape, higher particle density or higher liquid water content results in higher Z_{DR}. The differential phase shift Φ_{DP} measures the phase difference (in degrees) between the forward-propagating horizontally polarized wave and the vertically polarized wave. As the signals propagate through a medium such as rain, the horizontally polarized wave gradually slows down relative to the vertically polarized wave as it encounters more liquid water because raindrops are oblate. This slowing results in a positive phase difference between the waves. The range derivative of this differential phase shift is the specific differential phase, K_{DP} (given in deg km^{-1}), which is sensitive to the concentration of liquid drops but is nearly zero for heavily aggregated snow or dry graupel/hail. As a consequence,

Corresponding author address: Matthew R. Kumjian, CIMMS/NSSL, National Weather Center, 120 David L. Boren Blvd., Norman, OK 73072.
E-mail: matthew.kumjian@noaa.gov

DOI: 10.1175/2008JAS2815.1

© 2009 American Meteorological Society

K_{DP} is a good indicator of liquid water content in the resolution volume. The correlation coefficient between the backscattered returns at horizontal and vertical polarization at zero lag time ρ_{HV} is sensitive to the diversity of particle sizes, orientations, shapes, and phase compositions within the sampling volume, being especially sensitive to particles of the size in which resonance scattering effects occur. Such resonance scattering occurs when the ratio

$$\Re = \frac{D\sqrt{|\varepsilon|}}{\lambda} \tag{1}$$

is on the order of unity (where D is the particle equivolume diameter, ε is the dielectric constant of the particle, and λ is the radar wavelength).

b. Microphysical processes

Polarimetric variables are especially sensitive to microphysical processes characterizing particle phase transitions (e.g., melting) and size sorting of hydrometeors. Signatures from precipitating systems evident in the polarimetric data subsequently provide information about these microphysical processes. The polarimetric signature of a melting layer is an example of the snow-to-rain transition (melting) that appears distinctly in the observed variables (see Ryzhkov and Zrnić 1998; Brandes and Ikeda 2004; Giangrande et al. 2005, 2008).

The trajectories of hydrometeors are dependent on airflow patterns within the storm. Because the terminal fall speed of a raindrop increases monotonically with its diameter (Gunn and Kinzer 1949), drops will be advected throughout the storm at varying rates. A consequence of this is a separation of drops based on their size because smaller drops are advected farther downstream than larger drops, which fall faster and thus are exposed to air currents for shorter time intervals. This separation of drop sizes due to a combination of air motions in storms and different terminal fall speeds is what we define as size sorting.

c. Size sorting

Generally, Z_{DR} increases with Z_{HH} in rain. However, Z_{DR} can vary dramatically for a given Z_{HH} because of strong local drop size distribution (DSD) variability, which is related directly to size sorting. In this subsection we describe several size sorting mechanisms found in convective storms.

Differential sedimentation, the simplest size sorting mechanism, occurs in the absence of any air motion. When a cloud begins to precipitate, the largest drops fall faster than the smaller drops. Before an equilibrium drop size distribution is attained, the median drop size increases with decreasing height. As a result, polarimetric observations of developing convective cells generally display enhanced Z_{DR} beneath the cell, often collocated with very low Z_{HH}.

Positive vertical velocities in convective updrafts provide additional size sorting to the differential sedimentation mechanism. As hydrometeors encounter upward air motion, their fall velocities are affected. If the updraft vertical velocity is greater than the hydrometeor terminal velocity, the particle is lofted. Only if the terminal velocity of the hydrometeor is greater than the vertical velocity will the particle fall. Size sorting within updrafts is frequently observed in convective storms as a Z_{DR} column (e.g., Caylor and Illingworth 1987; Illingworth et al. 1987; Tuttle et al. 1989; Meischner et al. 1991; Conway and Zrnić 1993; Brandes et al. 1995; Hubbert et al. 1998; Kennedy et al. 2001; Loney et al. 2002; Ryzhkov et al. 2005; Kumjian and Ryzhkov 2008). Only the largest raindrops that have large terminal velocities can fall through the updraft; the other drops are carried farther aloft. If the storm updraft is so intense that no raindrops can fall, the largest drops fall at the periphery of the updraft, where vertical velocities are diminished. In this case, the Z_{DR} column is situated at the edge of the updraft, usually along a gradient of Z_{HH}.

Strong rotation on the scale of a tornado can cause size sorting through centrifuging of hydrometeors (e.g., Dowell et al. 2005). In the case of rain, the largest drops are centrifuged outward farther than the smaller drops. A pattern of concentric bands of Z_{HH} and an outer band of enhanced Z_{DR} in a study by Bluestein et al. (2007) are likely a manifestation of this type of size sorting. In a mesocyclone, the length and velocity scales are such that centrifuging of raindrops is less significant; centrifugal accelerations are roughly two orders of magnitude lower for characteristic mesocyclone scales than for characteristic tornado scales.

Size sorting has been attributed to wind speed shear for several decades (e.g., Gunn and Marshall 1955; Hitschfeld 1960; Jameson and Johnson 1983). Precipitation particles approximately follow the horizontal flow for modest wind speeds. In the event of extremely strong winds such as in a tornado, the raindrops do not follow the air currents. In fact, Dowell et al. (2005) found large differences between the air trajectories and the hydrometeor trajectories in a tornado, which can lead to significant errors in Doppler velocity retrievals. The particles that fall more slowly will experience horizontal advection longer than larger particles falling faster. In linear mesoscale convective systems, an enhancement of Z_{DR} is found frequently along the leading edge. Size sorting due to a combination of quasi-unidirectional

wind shear and the leading convective updrafts produces this enhancement.

In supercells, Kumjian and Ryzhkov (2008) have found that numerous signatures are consistently observed in the polarimetric data, including the tornadic debris signature, signatures of large hail, low-level inflow and the midlevel updraft, Z_{DR} and K_{DP} columns, midlevel Z_{DR} and ρ_{HV} rings, and the low-level Z_{DR} arc. This study examines the last signature in detail, which appears to be caused by the size sorting of raindrops due to speed and directional wind shear. Strong increases in speed and clockwise turning of the winds with height characterize helical environments (i.e., those with helicity; Lilly 1986). Within rotating updrafts, vertical helicity can be quite large. In contrast, vertical helicity is assumed to be negligible when we consider the storm-relative environmental helicity, which is a measure of the streamwise component of the vorticity of the environmental flow in the reference frame of the storm (Davies-Jones 1984). Davies-Jones et al. (1990) define storm-relative environmental helicity (SRH) as

$$\mathrm{SRH} = \int_0^{h'} (\nabla \times \mathbf{v}_H) \cdot (\mathbf{v}_H - \mathbf{v}_c)\, dz, \qquad (2)$$

where the integration typically is performed from the ground to some height h', generally taken to be the level of free convection or about 3 km (e.g., Droegemeier et al. 1993; Markowski et al. 1998). The horizontal velocity vector $\mathbf{v}_H$ and the storm motion vector $\mathbf{v}_c$ are used in the integrand. Numerous studies have found that the low-level SRH is a decent indicator of the potential for tornadoes and can be an important prognostic variable for severe storm forecasters (e.g., Leftwich 1990; Davies and Johns 1993; Colquhoun and Riley 1996; Kerr and Darkow 1996; Rasmussen and Blanchard 1998; Thompson et al. 2003, 2007). Thus, it is important to obtain accurate estimates of the low-level SRH, which is known to have significant spatial and temporal variations (e.g., Davies-Jones 1993; Markowski et al. 1998). Because soundings are infrequent and are only meant to capture the synoptic-scale environment, often they are not adequate to resolve the storm-scale variability of SRH. Richardson et al. (2007) found that heterogeneities within the mesoscale environment can also be important, at least in numerical simulations. These mesoscale inhomogeneities would not be captured by sparse and infrequent soundings.

The next section will describe the Z_{DR} arc and the size sorting that causes it in more detail and presents a hypothesis relating the Z_{DR} arc and low-level SRH. In section 3, we present a simple numerical model used to test the hypothesis and provide results from several experiments. Observations from tornadic and nontornadic supercells as well as nonsupercell severe storms are discussed in section 4. Section 5 provides a summary of the conclusions from this work.

2. The Z_{DR} arc

a. Description

The Z_{DR} arc is a narrow arc-shaped region of very high Z_{DR} values (>4 dB) found along the Z_{HH} gradient of the southern (right) or inflow edge of the forward-flank downdraft (FFD) echo in right-moving supercell storms (Kumjian and Ryzhkov 2008). It extends from the updraft region (and thus sometimes connects to the Z_{DR} column) downstream along the edge of the FFD echo, generally aligned in a direction roughly parallel to the storm motion. This region of the storm is characterized by relatively low Z_{HH} and high Z_{DR}, which indicate the presence of a sparse population of large (6–8 mm) drops and a relative lack of smaller drops. The signature is generally very shallow, located in the lowest 1–2 km of the storm. For comparison, the typical environmental melting level in the spring cases is about 3–4 km. Such a signature has been observed at S, C, and X bands in many supercells from different geographic regions, including the High Plains (Van Den Broeke 2007, personal communication), the Southern Plains (Kumjian and Ryzhkov 2008; Snyder 2008), the southeastern United States (Kumjian et al. 2008), southern Finland (Outinen and Teittinen 2007, 2008), Canada (Kumjian and Ryzhkov 2007), and Germany (Höller et al. 1994). The Z_{DR} arc has also been seen in most seasons, as early as 1 March and as late as 10 November. We expect the Z_{DR} arc to be present in winter supercells when polarimetric observations become more widely available. Several examples of Z_{DR} arcs observed in central Oklahoma are presented in Fig. 1. In the figure, the data from the original polar radar coordinates have been linearly interpolated onto a Cartesian grid. The Z_{DR} arc is a consistent feature of supercells and thus may be related to intrinsic processes both within the storms and in their environments.

b. Size sorting hypothesis

Some of the earliest studies of supercell structure noted that the sloping reflectivity echo overhang in the forward flank is a manifestation of precipitation particles being advected toward the left flank of the storm (e.g., Browning and Donaldson 1963; Browning 1964, 1965). Browning (1964) alluded to wind shear as a size sorting mechanism by suggesting that smaller particles

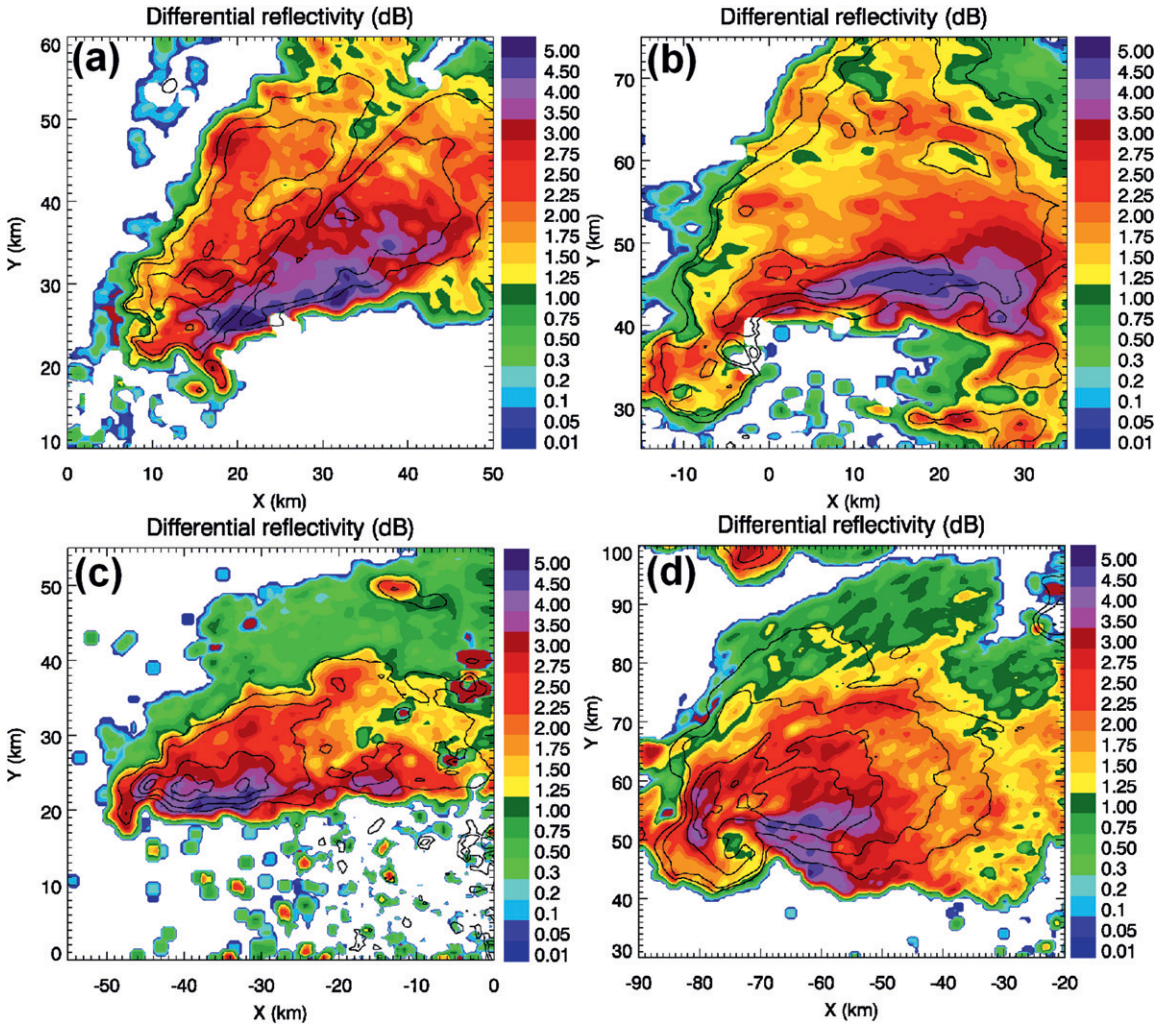

FIG. 1. Examples of the Z_{DR} arc signature in four supercell storms observed by the KOUN S-band polarimetric radar, with Z_{DR} values in dB. The 30-, 40-, 50-, and 55-dBZ contours of Z_{HH} are overlaid. The supercells were observed on (a) 2234 UTC 8 May 2003 at 1.5° elevation, (b) 0333 UTC 10 May 2003 at 0.5° elevation, (c) 2346 UTC 26 May 2004 at 0.4° elevation, and (d) 0044 UTC 30 May 2004 at 0.5° elevation. In each case a strong enhancement of Z_{DR} (values in excess of 4 dB) is found along the Z_{HH} gradient on the right forward flank (inflow side) of the storm.

are transported farther downstream than larger hydrometeors. Additionally, he studied cyclonic ''streamers'' of precipitation that indicated hydrometeors falling into an environment in which winds veered with height.

In supercell storms, size sorting can be extreme. The strong speed and directional shear that is common in low-level storm-relative hodographs of tornadic supercell environments (e.g., Maddox 1976; Davies-Jones 1984; Thompson and Edwards 2000; Thompson et al. 2003; Esterheld and Giuliano 2008) can cause a significant amount of drop sorting in a relatively shallow layer, resulting in a substantially modified drop size distribution along the edge of the precipitation echo on the inflow side of the storm (i.e., the FFD). This modified DSD contains large drops and a relative lack of smaller drops, which have been advected farther into the FFD. Polarimetric radar observations reveal such skewed DSDs to be strong enhancements of Z_{DR} because the median drop size is quite large. Additional evidence for strong shear affecting supercell precipitation at low levels comes from a recent study by Yu et al. (2009), who found unusual dual-peak signatures in the Doppler spectra from one of the tornadic supercells considered in the current study[1] (10 May 2003). They attributed

[1] The dataset used in this study is the same one used in Kumjian and Ryzhkov (2008). Details of the cases can be found in that paper.

these spectral signatures (which were confined to the lowest elevation angles) to strong shear within the radar sampling volume. Using a simple simulation with vertical shear on the order of 0.01 s^{-1}, they were able to reproduce the observed spectra fairly well.

Ryzhkov et al. (2005) first proposed size sorting as a physical explanation for the significant enhancement of Z_{DR} found along the FFD of supercells. Strong low-level shear contained in a shallow layer would promote significant size sorting in that shallow layer. In the Yu et al. (2009) study, the lowest elevation angle scans sampled the storm in the lowest 1 km, consistent with the shallow depth of the Z_{DR} arc signature. We suggest that the Z_{DR} arc location and shape are indicative of a wind shear profile most commonly associated with supercells (Fig. 2).

Previous studies (e.g., Goddard et al. 1982; Wakimoto and Bringi 1988) and T-matrix calculations have shown that the intrinsic Z_{DR} of the largest (6–8 mm) raindrops at S band exceeds 4 dB. Although these large drops are found in convective storms, they are usually associated with much higher concentrations of smaller drops, decreasing their relative contribution to the backscattering characteristics observed by the radar. Thus, in heavy rain Z_{DR} generally does not exceed 2–3 dB. However, if these smaller drops are largely removed from the DSD, the observed Z_{DR} can increase to 4–5 dB (and Z_{HH} and K_{DP} would be relatively low). The resulting DSD is quite exotic, as shown by Schuur et al. (2001) in 2D video disdrometer data collected beneath the Z_{DR} arc region of a supercell. Vigorous size sorting is necessary for this type of significant separation of drop sizes. We argue that the low-level inflow-enhanced veering wind shear characteristic of supercell environments is the size sorting mechanism that causes the Z_{DR} arc signature to appear and that the degree of size sorting is related to the low-level SRH. The next section develops a simple numerical model to explore this hypothesis and to quantify the impact of size sorting on polarimetric variables for a given DSD.

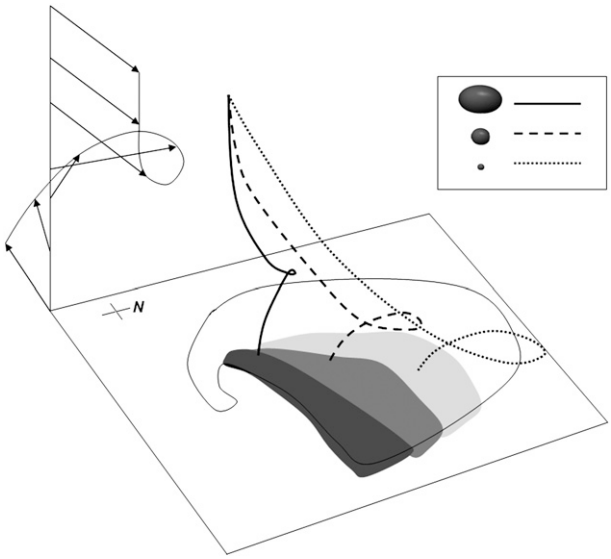

FIG. 2. Schematic depiction of how low-level veering winds in a supercell storm-relative frame lead to an enhancement of Z_{DR} along the right (inflow) edge of the forward-flank downdraft precipitation echo (outlined on the surface). The wind vectors indicate the veering flow. If projected onto a horizontal plane, the line connecting the wind vectors would represent the hodograph, the area of which is proportional to the low-level SRH. Cyclonic trajectories are shown for large drops (black solid line), medium sized drops (dashed line), and small drops (dotted line) falling from a point source. The shading represents the Z_{DR} enhancement, which is maximized at the edge of the forward-flank downdraft.

3. The model

a. Description

To test the hypothesis, a simple model of a precipitating cloud was constructed. The domain has variable horizontal extent, depending on what is necessary to capture the entire precipitation field after it is advected. The domain extends 3 km in the vertical. Horizontal resolution is 500 m and vertical resolution is 200 m. A 3 km × 3 km cloud is placed at the top of the domain. The cloud is square with truncated corners. A Marshall–Palmer raindrop size distribution is assumed initially in the cloud. The rainfall rate in the cloud is modulated such that the center of the cloud is characterized by a rainfall rate of 50 mm h^{-1}; this decreases to 35 mm h^{-1} moving away from the center and is 25 mm h^{-1} at the edges. The DSDs are discretized into 80 size intervals, ranging from 0.05 to 7.95 mm in 0.1-mm increments. Drop sizes are treated independently as ''packets'' of like drops filled with a concentration prescribed by the initial DSD. The domain grid boxes occupied by the cloud are subdivided into these 100 m × 100 m (× 80 drop sizes) packets. No drop interactions are considered, so the trajectories of drops of each size interval are calculated independently. At the initialization of the model the cloud begins to rain, and thus each packet (containing a concentration of drops as determined by the DSD) falls into the domain. The vertical extent of each packet is given by the distance that the particular drop size falls in one time step, which in this study is Δt = 5 s. This time step was chosen to maximize the computational efficiency while keeping the solutions numerically stable. Terminal velocities are given by a synthesis of the models developed by Atlas and Ulbrich (1977) and Atlas et al. (1973):

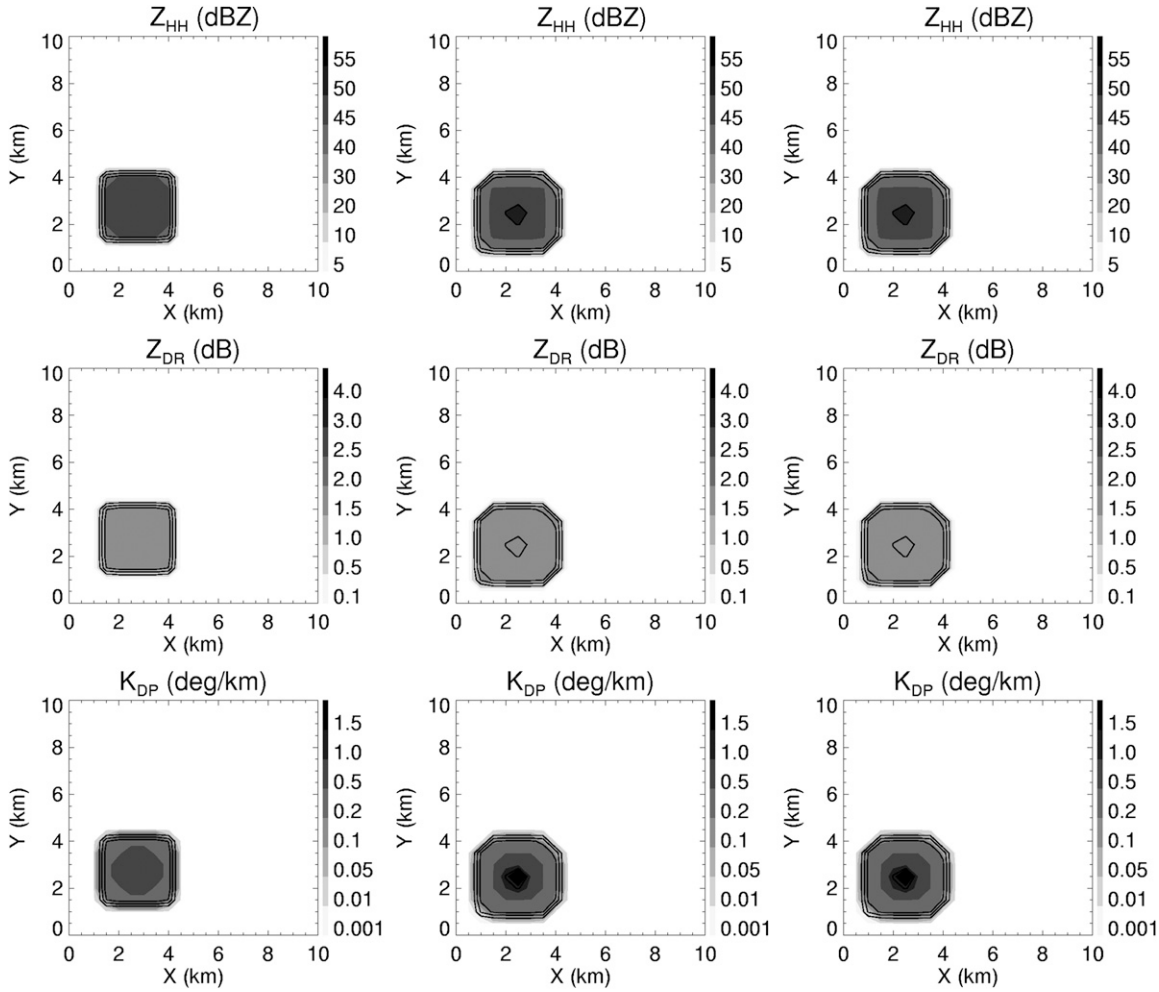

FIG. 3. Resulting polarimetric fields from the control experiment (experiment 0). From top to bottom, the polarimetric variables are Z_{HH}, Z_{DR}, and K_{DP}. From left to right the columns show CAPPIs from 3 km, 1500 m, and 400 m. No modification in the variables due to advection is observed. Slight differences are due to the smoothing, which results in coarser resolution.

$$(v_t)_n = \begin{cases} 3.78 D_n^{0.67} & \text{for } 0.05 \le D_n \le 3.05\,\text{mm} \\ 9.65 - 10.3\exp(-0.6 D_n) & \text{for } D_n > 3.05\,\text{mm} \end{cases}, \tag{3}$$

where the subscript n represents the nth drop size interval and D is in mm. The sensitivity of the model to the initial DSD is discussed in a later subsection.

A new set of packets is placed at the top of the domain at each time step, thus allowing for a continuous flux of drops. The packets of raindrops fall into a horizontally homogeneous wind field. Any vertical profile of wind can be administered. Hodographs displaying the wind profiles will be shown with the results of each experiment. As the packets of drops fall, they are advected with the horizontal flow. The location of each packet and drop size at each time step is calculated. After allowing the precipitation to attain a steady state (approximately 3000 s), constant altitude plan position indicators (CAPPIs) are constructed for various heights. Packets of drops in the corresponding grid boxes are accounted for. This gives the concentration of drops of all sizes, or the modified DSD, at the chosen altitude. From this modified DSD, a T-matrix method (Mishchenko 2000) is employed to calculate the polarimetric variables Z_{HH} (dBZ), Z_{DR} (dB), and K_{DP} (deg km^{-1}). At the S band in pure rain, ρ_{HV} does not differ much from unity and thus is not calculated for these simulations.

In addition to drop interactions, other physical processes have been omitted from the model, including evaporation and spontaneous breakup. For the values of Z_{HH} selected in the model, evaporation is not significant. In general, evaporation occurs most rapidly for smaller drops; when uninhibited, the DSD is narrowed,

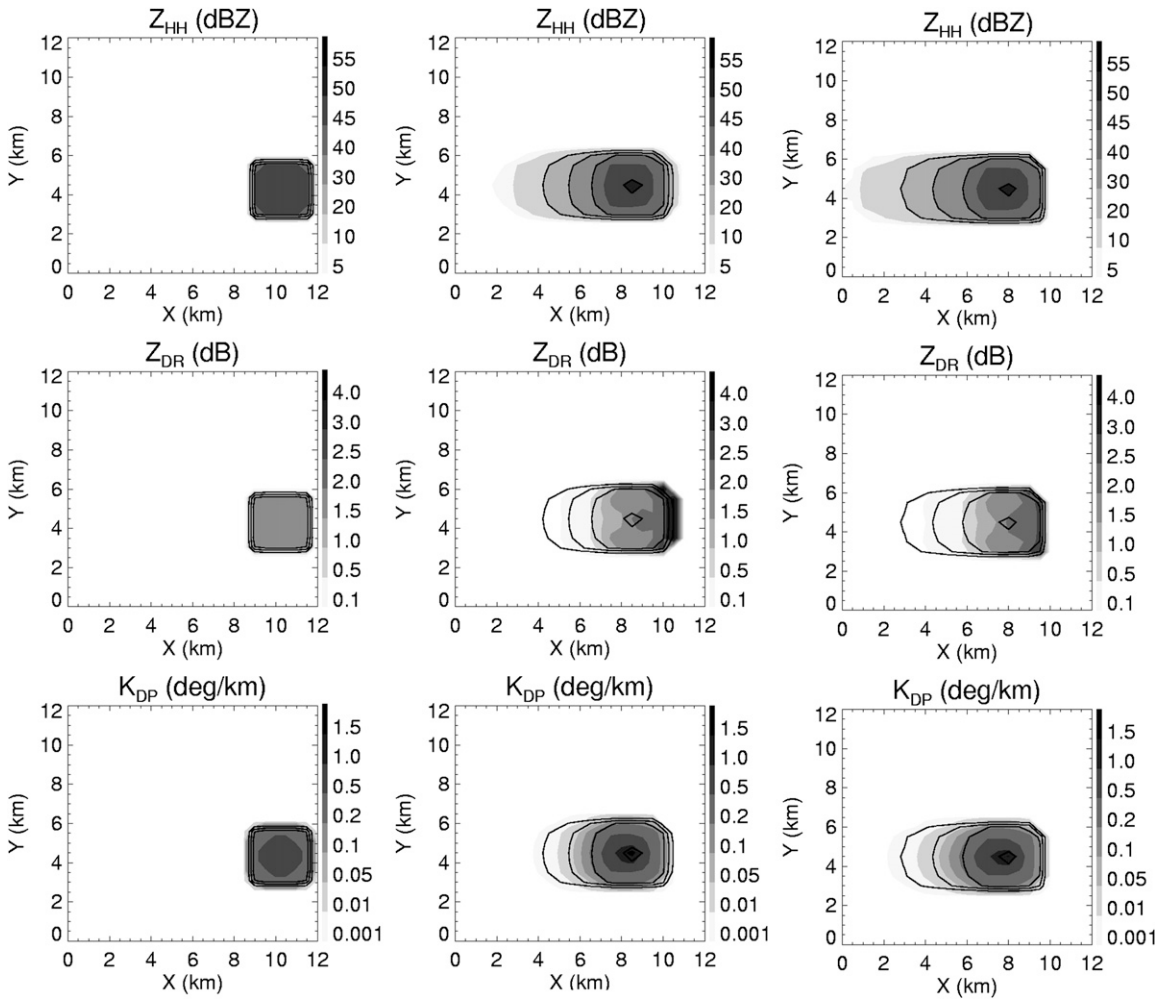

FIG. 4. Results from the first experiment with a unidirectional shear case. The enhancement of Z_{DR} is located on the leading edge of the eastward-moving storm and is analogous to similar enhancements observed in linear mesoscale convective systems. Subsequently, this signature would not be considered a Z_{DR} arc, and there is no relation between the magnitude of Z_{DR} and SRH (which is 0 in this case).

favoring the larger drop sizes. This would lead to a larger median drop size in the radar resolution volume, enhancing Z_{DR}. Spontaneous breakup of the largest drops would decrease the relative number of large drops and thus decrease Z_{DR}. However, very large (6–8 mm) raindrops have been observed in convective storms (Schuur et al. 2001), so spontaneous breakup is probably not a significant factor in this case; or perhaps it is balanced by self-collection, as suggested by Romine et al. (2008). The modeled precipitation is assumed to fall at terminal velocity from the initialization, which neglects the brief acceleration that drops experience if starting from rest. Beard (1976) shows that the response time of a raindrop to changes in drag is on the order of $v_t(D)/g$, or about 1 s, where $v_t(D)$ is the terminal velocity of a raindrop with diameter D and g is the gravitational acceleration. This assumption results in an error on the order of a few meters, which is negligible compared to the relatively coarse resolution of the model. The drops are assumed to follow the horizontal winds perfectly, which (as mentioned above) is not true in cases of extreme winds. So, for the relatively coarse model resolution and the magnitude of the wind speeds prescribed in the experiments herein, the errors due to the assumption that raindrops instantaneously adjust to the wind field are negligible.

b. Results

The results from the simulations are presented in this subsection. First, a control experiment is performed in which the raindrops fall into a domain with no wind. We expect the resulting fields of polarimetric variables to be

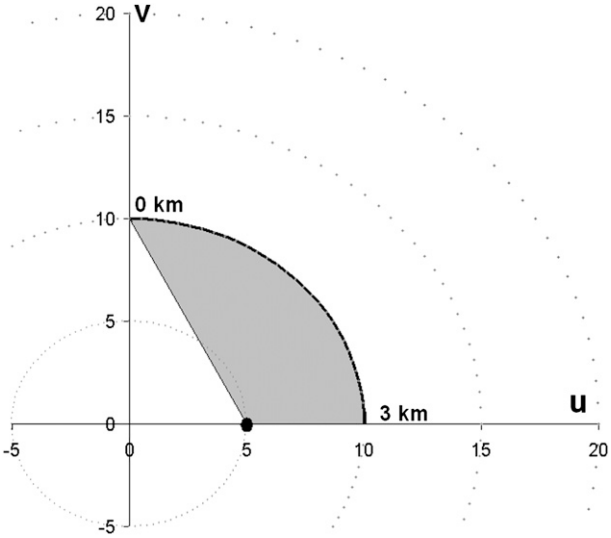

FIG. 5. Hodograph used in experiment 2. The u and v components of the idealized wind field are displayed on the axes. Wind speeds are given in m s^{-1}. The solid black line traces the tip of the environmental wind vector from the surface (labeled as 0 km) to the top of the domain (labeled as 3 km). The large black dot represents the tip of the storm motion vector, which is 5 m s^{-1} toward the east in this case. The gray shaded area is proportional to the 0–3-km SRH.

largely unchanged from the original profile, except for minor differences incurred by the smoothing process, which results in coarser resolution than the individual packets. Indeed, the calculated magnitudes of the polarimetric variables at 1500 and 400 m are quite similar to the initial state (Fig. 3). The results from each experiment will be presented in nine panels, as in Fig. 3. No enhancement of Z_{DR} is evident along the edges of the cell because of the absence of a size sorting mechanism. The slight difference in appearance is due to the additional smoothing that takes place in the calculations and contouring (i.e., the enhancement at the center of the echo occurs because more than one packet of drops is found in those grid boxes).

A unidirectional shear profile is prescribed in the first experiment. The environmental winds are westerly at all levels, increasing from 1 m s^{-1} at the surface to 15 m s^{-1} at 3 km. The storm is moving toward the east at 15 m s^{-1}. As a result, the storm-relative wind profile is unidirectional and from the east, increasing in magnitude with decreasing height. This type of wind profile can be found in environments of mesoscale convective systems in the Great Plains, for example. The results from this experiment show that the precipitation fields have been modified by the wind shear. Raindrops are advected downstream (which is toward the west in the storm reference frame). As a result of the advection, the Z_{HH} echo extends westward. In Fig. 4, a strong enhancement of Z_{DR} is seen along the right edge of the storm, which corresponds to its leading edge. This enhancement is oriented perpendicular to the direction of motion and frequently is augmented by the convective updrafts in real storms. The alignment and location of this enhancement is distinct from that described for the Z_{DR} arc in supercells and thus would not be considered a Z_{DR} arc. Recall that the Z_{DR} arc is located on the front right edge of the FFD precipitation echo and is generally aligned approximately parallel to storm motion. Subsequently, we should not expect any relation between the magnitude of Z_{DR} and the low-level SRH, which is 0 in this experiment.

Next, an idealized veering wind profile is prescribed. The profile is presented using a hodograph, showing the u and v components of the wind field at each level (Fig. 5). At the surface, winds are from the south at 10 m s^{-1} and uniformly veer with height to westerly at 3 km, also at 10 m s^{-1}. However, this time the precipitating cloud moves toward the east at 5 m s^{-1}, as indicated by the black dot. This introduces speed shear and enhances the veering. The SRH is proportional to the area swept out by the hodograph (Davies-Jones et al. 1990; Droegemeier et al. 1993) and is shaded in gray. The representativeness of such idealized profiles considered herein is discussed in a later subsection. The resulting polarimetric fields are clearly modified by the winds at both 1500 and 400 m (Fig. 6). The precipitation echo from Z_{HH} extends downstream, indicating that drops are being advected by the winds. In the Z_{DR} field, an enhancement is present along the southern edge of the storm, aligned parallel to storm motion. Maximum values of Z_{DR} at 400 m are about 3.6 dB. Note that K_{DP} is largest in the center of the storm, closely associated with the highest Z_{HH}. This is expected because rainfall rate is nearly linearly related to K_{DP} (Sachidananda and Zrnić 1987). The Z_{DR} enhancement occurs along the gradient in reflectivity, indicating a sparse population of larger drops with a lack of smaller drops, as observed in real storms.

The wind shear is amplified in experiment 3, with a 15 m s^{-1} flow from the south at the surface veering to westerly at 15 m s^{-1} at 3 km in the idealized quarter-circle hodograph (Fig. 7). The storm motion vector is toward the east at 10 m s^{-1}, enhancing the speed and directional shear relative to the previous experiment, thereby also enhancing the SRH. The resulting polarimetric variables show further modification due to advection (Fig. 8). The Z_{HH} echo extends farther downstream, and the Z_{DR} arc at 400 m is quite strong, with maximum values about 4.5 dB. Again, K_{DP} closely follows the Z_{HH} pattern. Also of note is that the enhancement of Z_{DR} is quite shallow; the Z_{DR} field at 1500 m shows only a 0.5-dB increase over the

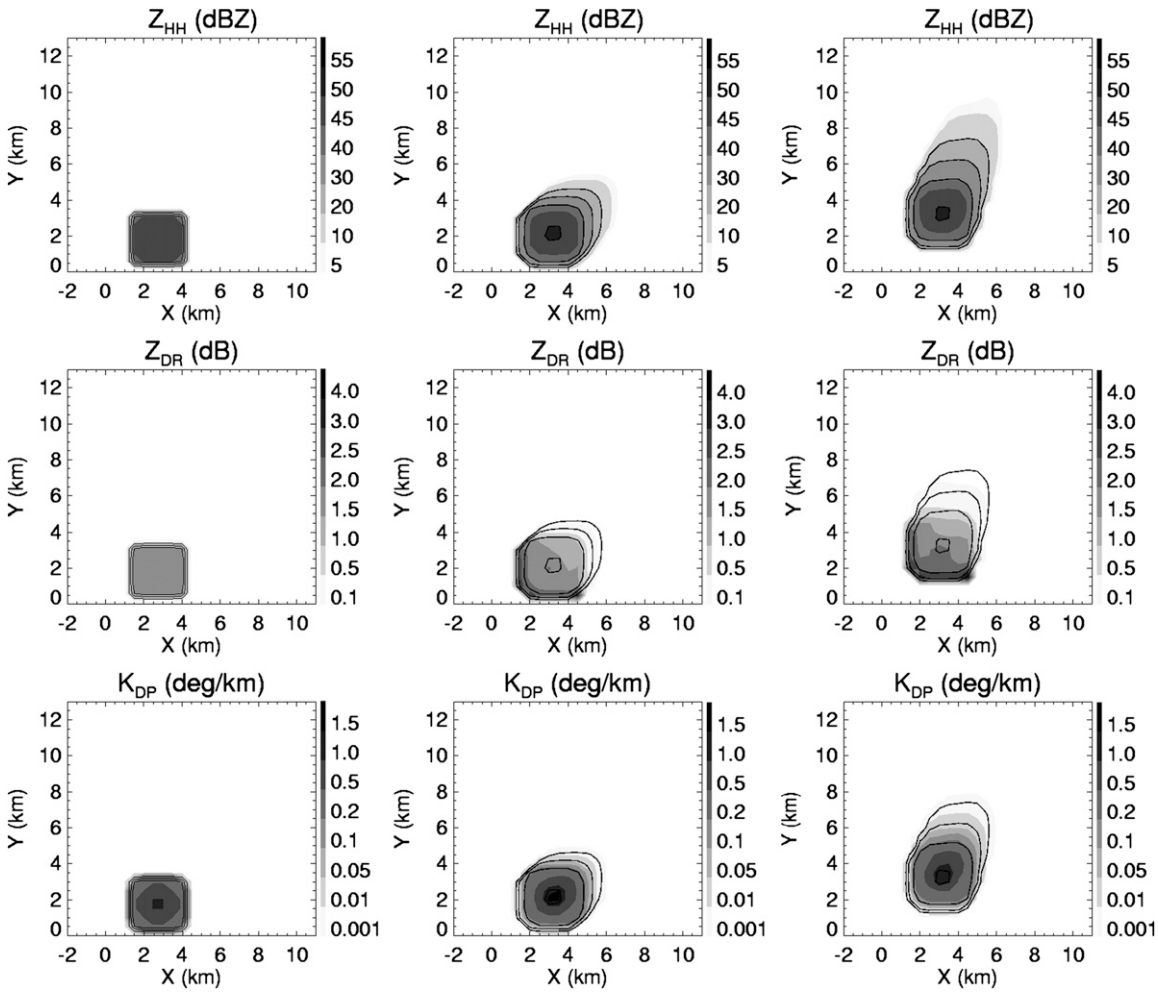

FIG. 6. As in Fig. 4, but for the resulting polarimetric fields from experiment 2 using the idealized hodograph in Fig. 5. An enhancement in Z_{DR} is found on the southern edge of the precipitation echo at 400 m, with maximum values about 3.6 dB.

initial state. The greatest enhancement of Z_{DR} occurs below this level, in the lowest 1 km of the domain. This agrees well with the observations of the Z_{DR} arc, in which the enhancement is only found in the lowest 1–2 km above the ground.

The next experiment (4) uses the low-level wind profile from 9 May 2003, as observed by the 0000 UTC sounding from Norman, Oklahoma (KOUN). This sounding has large SRH and characterizes the environment of a tornadic supercell that produced a violent F-4 tornado in central Oklahoma. A detailed case study of this event can be found in Romine et al. (2008). Polarimetric observations from this storm display a strong Z_{DR} arc (Fig. 1a). The initialization uses linearly interpolated winds between the actual sounding observations to provide enough data points below 3 km. The hodograph is essentially unchanged by this interpolation, aside from minor smoothing (Fig. 9). Storm motion was determined by Esterheld and Giuliano (2008), who averaged the translational velocity of the precipitation echo in the volume scans leading up to and just after tornadogenesis, encompassing the time of the polarimetric data from this storm shown above. The resulting polarimetric fields are modified by the shear, again producing an enhancement of Z_{DR} along the southern and eastern edges of the Z_{HH} echo (Fig. 10). The maximum Z_{DR} in the simulation is 4.5 dB, which agrees fairly well with the observed values in the Z_{DR} arc from this storm (4–5 dB). The orientation of the simulated enhancement is also in agreement with the observed signature.

c. *Impact of the initial DSD*

To some extent, the modeling results depend on the type of initial DSD aloft. Initially we assumed that the DSD aloft is a Marshall–Palmer distribution. The three-parameter gamma distribution

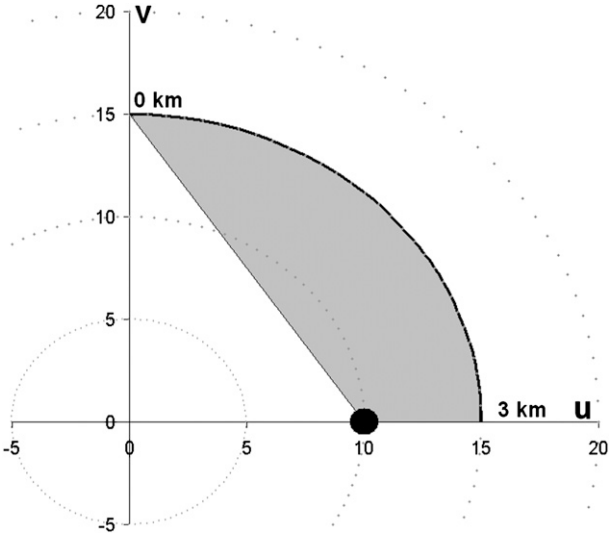

FIG. 7. As in Fig. 5, but for the idealized 0–3-km hodograph used in experiment 3. Storm motion is toward the east at 10 m s^{-1}.

$$N(D) = N_0 D^{\mu} \exp(-\Lambda D) \tag{4}$$

describes a larger variety of DSDs in rain (e.g., Ulbrich 1983). The intercept of the gamma DSD (N_0) for the raindrops aloft does not affect Z_{DR} because it is a relative measurement. Hence, additional variability of Z_{DR} is caused by variations of the parameters Λ and μ. Brandes et al. (2004) found that Λ and μ are generally well correlated and introduced the constrained gamma DSD in rain. Cao et al. (2008) established that in Oklahoma storms the relation between Λ and μ has the form

$$\mu = -0.0201\Lambda^2 + 0.902\Lambda - 1.718, \tag{5}$$

where Λ is expressed in mm^{-1}.

In convective storms, the parameter Λ is primarily defined by Z_{HH}, which usually varies from about 40 to 50 dBZ in the downstream forward-flank precipitation region of supercells. It can be shown that Λ for these values of Z_{HH} changes within the interval between 1.7 and 2.9 mm^{-1}. Correspondingly, the parameter μ varies from -0.24 to 0.73, according to Eq. (5). To assess the impact of the initial DSD on the spatial distribution of Z_{DR} and its maximal value at the 400-m level, we performed simulations for these two combinations of the parameters Λ and μ.

We compare the simulated Z_{DR} maxima to the SRH for each of the experiments by plotting the maximum Z_{DR} against the low-level SRH calculated from the simulated hodographs. The 0.4–3-km SRH is used rather than the traditional 0–3-km SRH. This is because the lowest level where the polarimetric variables were calculated was 400 m, and in some cases considerable SRH existed below this level. Except for experiment 4, all simulations were prescribed with idealized quarter-circle hodographs of varying magnitudes, as in experiments 2 and 3 above. A summary of these numerical experiments is provided in Table 1. The scatterplot of maximum Z_{DR} versus 0.4–3.0-km SRH for these experiments is shown in Fig. 11. The small diamonds represent the simulations using an initial Marshall–Palmer DSD, the asterisks indicate results of simulations using the first gamma DSD (i.e., $\Lambda = 1.7$ mm^{-1}; $\mu = -0.24$), and the triangles correspond to the second gamma DSD ($\Lambda = 2.9$ mm^{-1}; $\mu = 0.73$). As Fig. 11 indicates, there is a strong correlation between the maximal Z_{DR} and low-level SRH regardless of the type of DSD aloft. For low-level SRH exceeding about 150 m^2 s^{-2}, the largest modeled Z_{DR} values are attained. Minimum SRH thresholds for mesocyclones have been reported at 157 m^2 s^{-2} in observed storms (Davies-Jones et al. 1990) and 250 m^2 s^{-2} for simulated supercells (Droegemeier et al. 1993). Despite the limitations of our simplistic model, the results indicate that most (if not all) supercells should exhibit a fairly strong Z_{DR} arc.

The DSD formed near the ground is primarily determined by the size sorting due to wind shear rather than the initial DSD aloft. Note that the variability of the DSD in convective storms is usually less than in most stratiform rain cases (Bringi et al. 2003). In convective cores, most of the rain is generated from the melting of graupel and hail with relatively high density, which does not vary much. Stratiform rain originates from snow with very high diversity in its density, depending on the degree of riming or aggregation. As a result, size distributions of rain melted from snow more often exhibit larger variability compared to convective rain.

d. Representativeness of the modeled wind profiles

Although the quarter-circle hodographs used in our simulations are idealized, we feel that these wind profiles are representative of the general type of directional and speed shear found in supercell environments. Such simplified hodographs are not without precedent; previous modeling studies have used such quarter-circle and half-circle profiles (e.g., Weisman and Klemp 1984; Droegemeier et al. 1993; Weisman and Rotunno 2000). Additionally, the observed sounding used in experiment 4 yielded similar results.

Unfortunately, some uncertainty exists as to how well even the observed soundings capture the near-storm environment, especially because the strong low-level inflow from the storm can alter the local wind profiles.

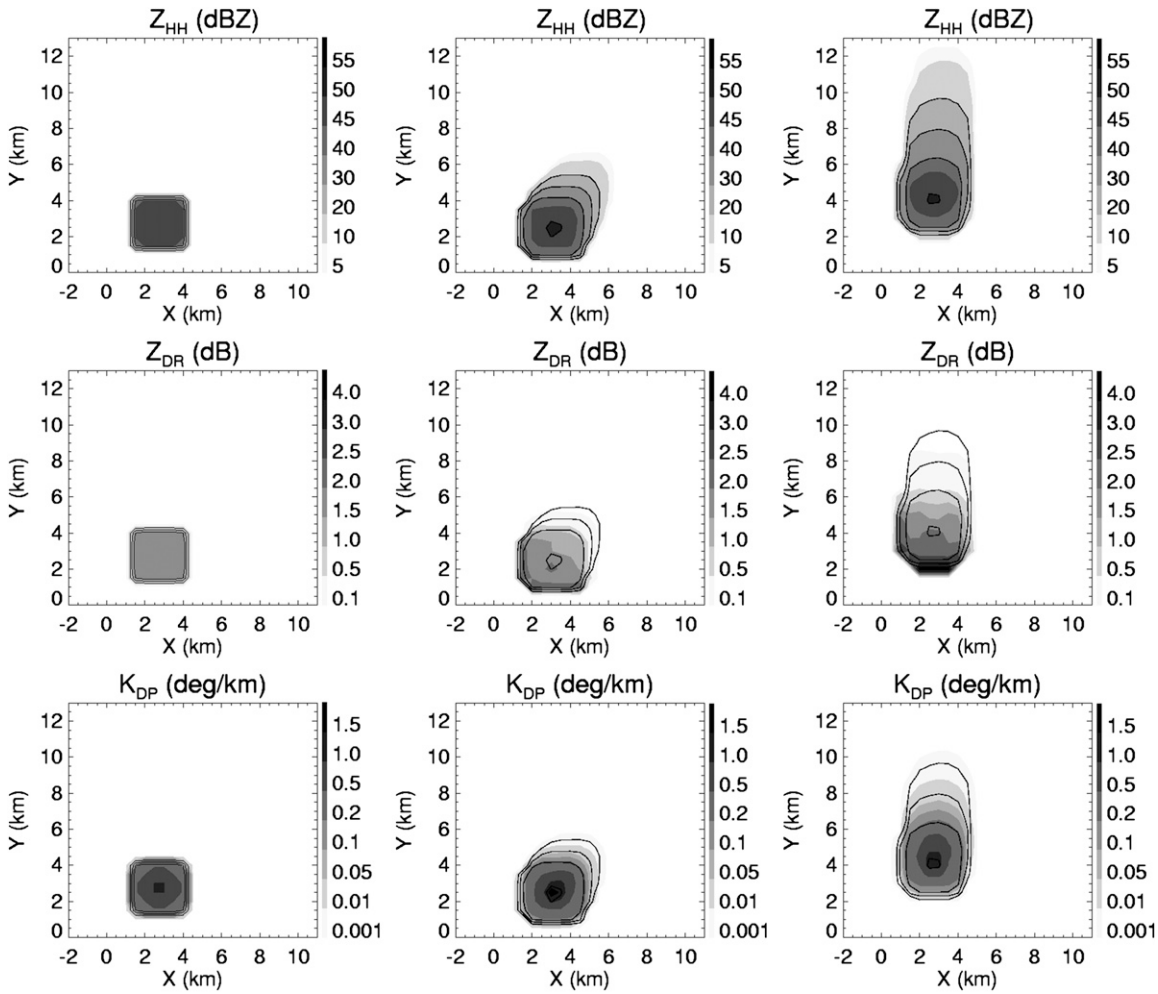

FIG. 8. As in Fig. 4, but for experiment 3 (the hodograph in Fig. 7). A substantial enhancement of Z_{DR} is present at 400 m, with maximum values about 4.5 dB.

In some cases, the inflow may intensify the low-level shear and SRH, which should increase the amount of size sorting. Observations within the near-storm environment are relatively sparse, so further studies are necessary to quantify the impact of the storm itself on its environment. This issue is further explored in the discussion section.

4. Observations

In this section we will describe observations of the Z_{DR} arc in tornadic and nontornadic supercells as it appears before the low-level mesocyclone occludes and once the occlusion takes place. Observations from left-moving supercells (resulting from the splitting of the parent storm) are presented. Additionally, the appearance of the signature in developing supercells and in nonsupercell storms preceding the development of severe weather is discussed briefly.

a. Supercell storms

1) PRE-OCCLUSION VERSUS OCCLUSION

The rear-flank downdraft (RFD) has long been implicated with tornadogenesis (e.g., Lemon and Doswell 1979). In fact, Davies-Jones (2008) has shown that the hook echo precipitation associated with the RFD can actually instigate tornadogenesis through the downward transport of air rich in angular momentum, which is subsequently converged under the updraft. Of particular interest in many modeling and observational studies is the occlusion of the low-level mesocyclone by the RFD, which is believed to be intricately tied to the development of a tornado (Lemon and Doswell 1979; Klemp and Rotunno 1983; Klemp 1987; Wicker and

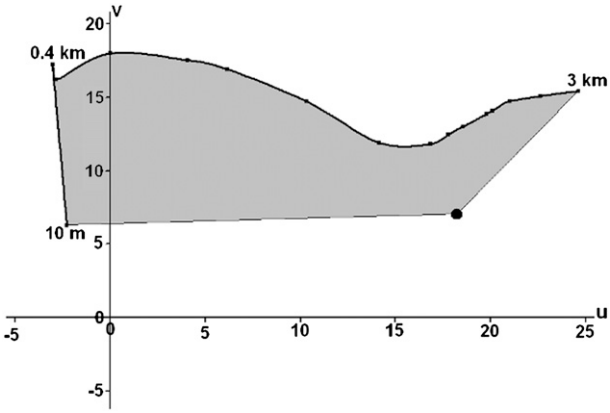

FIG. 9. As in Fig. 5, but for the observed 0–3-km KOUN hodograph from 0000 UTC 9 May 2003. This hodograph is used in the fourth experiment.

Wilhelmson 1995). Thus, any indication that the occlusion process is beginning may allow forecasters to give more advanced warnings. It should be noted, however, that the occlusion of the low-level mesocyclone is not a sufficient condition for tornadogenesis; recent research has shown that low-level thermodynamic characteristics of the RFD can be important (see Markowski 2002; Markowski et al. 2002, 2003).

A recent observational study by Van Den Broeke et al. (2008) suggests that the Z_{DR} arc tends to extend back toward the updraft at times leading up to tornadogenesis, sometimes wrapping around the inside of the hook echo (Kumjian et al. 2008). Observations of nontornadic supercells from the Kumjian and Ryzhkov (2008) dataset show this extension of the Z_{DR} arc preceding the occlusion of the low-level mesocyclone. Thus, it is unlikely that the Z_{DR} arc is a manifestation of

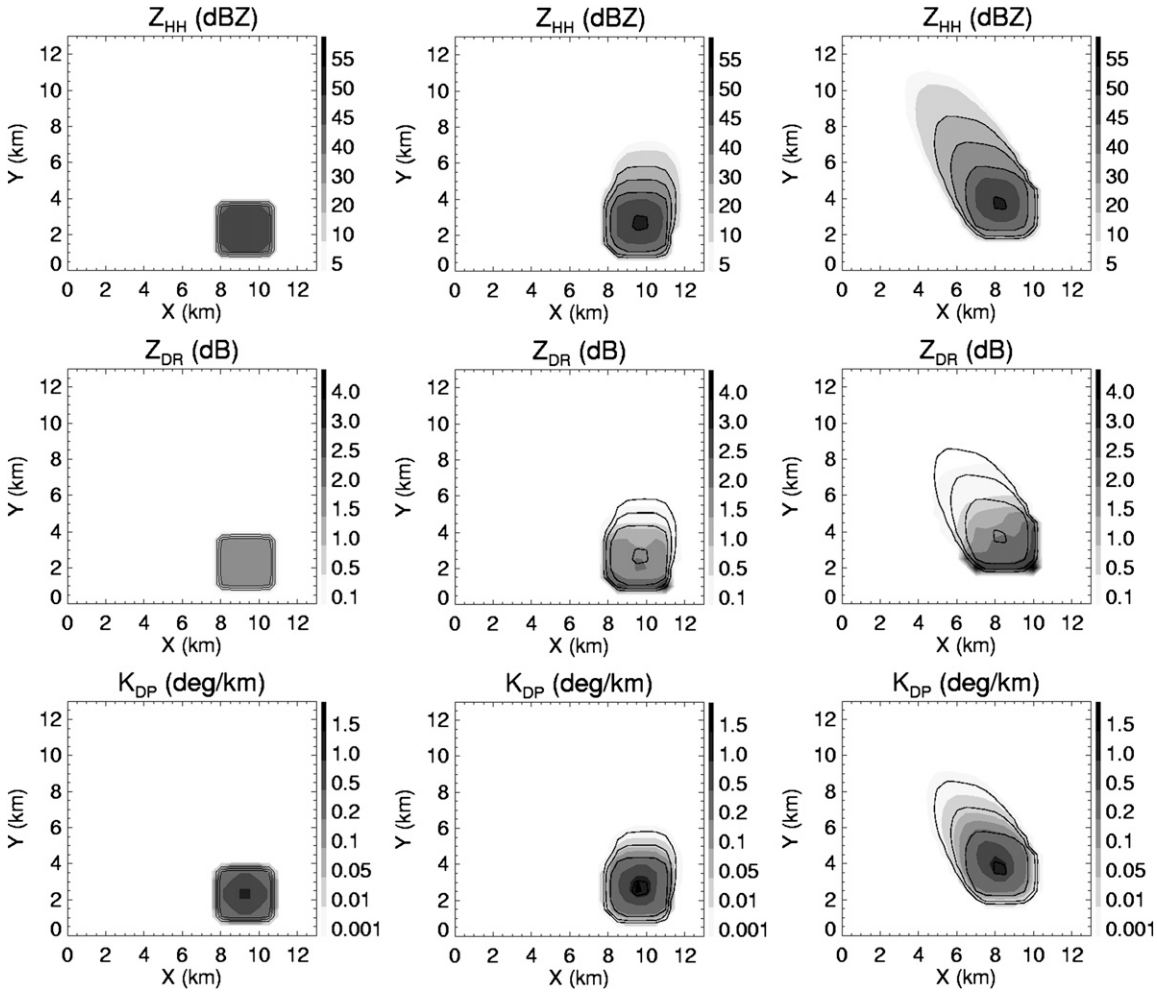

FIG. 10. As in Fig. 4, but for experiment 4 using the observed 0000 UTC 9 May 2003 KOUN hodograph (the hodograph in Fig. 9). The maximum Z_{DR} is about 4.5 dB.

TABLE 1. Summary of numerical experiments. The initial DSD aloft is given: MP (Marshall–Palmer), $\Gamma - 1$ (first gamma distribution with $\Lambda = 1.7\ \mathrm{mm}^{-1}$, $\mu = -0.24$), and $\Gamma - 2$ (second gamma distribution with $\Lambda = 2.9\ \mathrm{mm}^{-1}$, $\mu = 0.73$). The idealized wind profiles are indicated (the amplitudes of the quarter-circle hodographs are listed) along with the storm motion u and v components. The 0.4–3.0-km SRH calculated from the idealized hodographs and the maximum simulated Z_{DR} (dB) for each experiment are listed.

Experiment	DSD	Environmental shear profile	Storm motion (u, v) in m s^{-1}	0.4–3.0-km SRH	Maximum Z_{DR} (dB)
0	MP	No wind	(0, 0)	0	1.9
1	MP	Unidirectional shear	(15, 0)	0	4.2
2	MP	Quarter circle, 10 m s^{-1}	(5, 0)	87.2	3.6
3	MP	Quarter circle, 15 m s^{-1}	(10, 0)	159.4	4.5
4	MP	9 May 2003	(18.2, 7.0)	197.7	4.5
5	MP	Quarter circle, 2 m s^{-1}	(0, 0)	5.4	2.3
6	MP	Quarter circle, 3 m s^{-1}	(0, 0)	12.2	2.5
7	MP	Quarter circle, 6 m s^{-1}	(3, 0)	31.4	2.8
8	MP	Quarter circle, 7 m s^{-1}	(3, 0)	46.1	2.8
9	MP	Quarter circle, 10 m s^{-1}	(7, 0)	67.6	2.9
10	MP	Quarter circle, 10 m s^{-1}	(6, 0)	77.4	3.8
11	MP	Quarter circle, 10 m s^{-1}	(4, 0)	96.9	3.8
12	MP	Quarter circle, 10 m s^{-1}	(3, 0)	106.7	3.4
13	MP	Quarter circle, 10 m s^{-1}	(2, 0)	116.5	4.5
14	MP	Quarter circle, 10 m s^{-1}	(1, 0)	126.3	4.1
15	MP	Quarter circle, 10 m s^{-1}	(0, 0)	136.1	4.5
16	MP	Quarter circle, 15 m s^{-1}	(5, 0)	232.0	4.5
17	$\Gamma - 1$	No wind	(0, 0)	0.0	2.0
18	$\Gamma - 1$	Quarter circle, 7 m s^{-1}	(3, 0)	46.1	3.1
19	$\Gamma - 1$	Quarter circle, 10 m s^{-1}	(5, 0)	87.2	3.7
20	$\Gamma - 1$	Quarter circle, 10 m s^{-1}	(1, 0)	126.3	4.2
21	$\Gamma - 1$	Quarter circle, 15 m s^{-1}	(10, 0)	159.4	4.5
22	$\Gamma - 2$	No wind	(0, 0)	0	1.1
23	$\Gamma - 2$	Quarter circle, 7 m s^{-1}	(3, 0)	46.1	3.2
24	$\Gamma - 2$	Quarter circle, 10 m s^{-1}	(5, 0)	87.2	4.0
25	$\Gamma - 2$	Quarter circle, 10 m s^{-1}	(1, 0)	126.3	4.0
26	$\Gamma - 2$	Quarter circle, 10 m s^{-1}	(0, 0)	136.1	4.0

processes that instigate tornadogenesis. Instead, the extension toward the updraft may mark increased low-level inflow that augments the wind shear, coincident with increasing low-level vorticity that precedes the occlusion.

In contrast, the Z_{DR} arc often becomes ''disrupted'' by the hail signature, defined here as Z_{DR} values near 0 dB associated with Z_{HH} greater than 50 dBZ, once the occlusion takes place. The hail signature is a manifestation of large hailstones with statistically isotropic scattering properties that dominate the contributions from raindrops and smaller wet hailstones within the radar sampling volume (Fig. 12). Such hail signatures are quite common in the FFD core, especially in nontornadic supercells (Kumjian and Ryzhkov 2008). It appears as if the weakening of the updraft associated with the occlusion may diminish the low-level inflow, perhaps disrupting the size sorting that produces the Z_{DR} arc near the updraft.

Both tornadic and nontornadic supercells exhibit the Z_{DR} arc. However, there is some indication based on observations from KOUN that the Z_{DR} arc signature is disrupted more consistently in nontornadic supercells. It is possible that the consistent disruption of the Z_{DR} arc by a hail signature indicates that FFD outflow may be partially ''undercutting'' the updraft in a manner similar to that described by Brooks et al. (1993). This is because the hail signature marks a heavy precipitation core that has substantial amounts of liquid water inferred from very large K_{DP} values. Precipitation-induced drag, melting of hail and graupel, and evaporation of raindrops contribute to downward velocities, so these cores are generally associated with surface divergence. More observations are required to confirm or refute this suggestion, however; at present it remains speculative.

2) LEFT-MOVING SUPERCELLS

As convective storms develop midlevel rotation, dynamic effects due to the presence of vertical vorticity aloft promote updraft growth on the flanks of the storm, elongating and eventually splitting the main updraft (see Klemp and Wilhelmson 1978; Rotunno and Klemp 1982, 1985; Klemp 1987). This preferential growth on the flanks of the storm may lead the observed storm

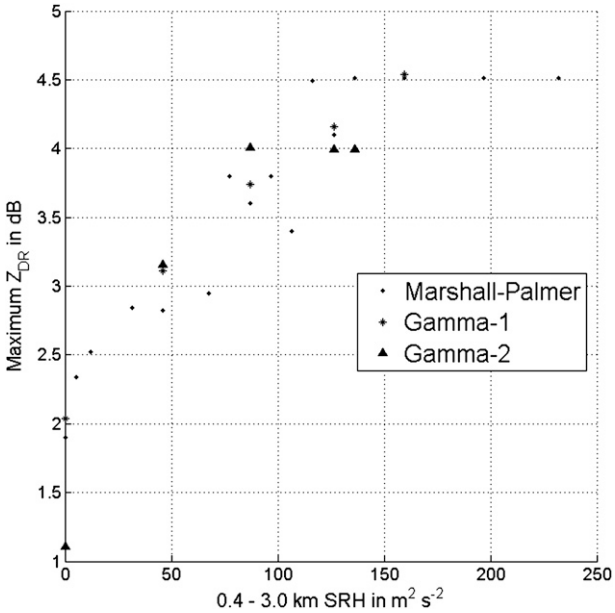

FIG. 11. Scatterplot of the 0.4–3-km SRH (m^2 s^{-2}) vs the maximum Z_{DR} value (dB) from the numerical experiments. A positive relation is evident. Different symbols correspond to different initial DSDs. Small diamonds indicate the Marshall–Palmer DSD; asterisks, the first gamma DSD; and triangles, the second gamma DSD.

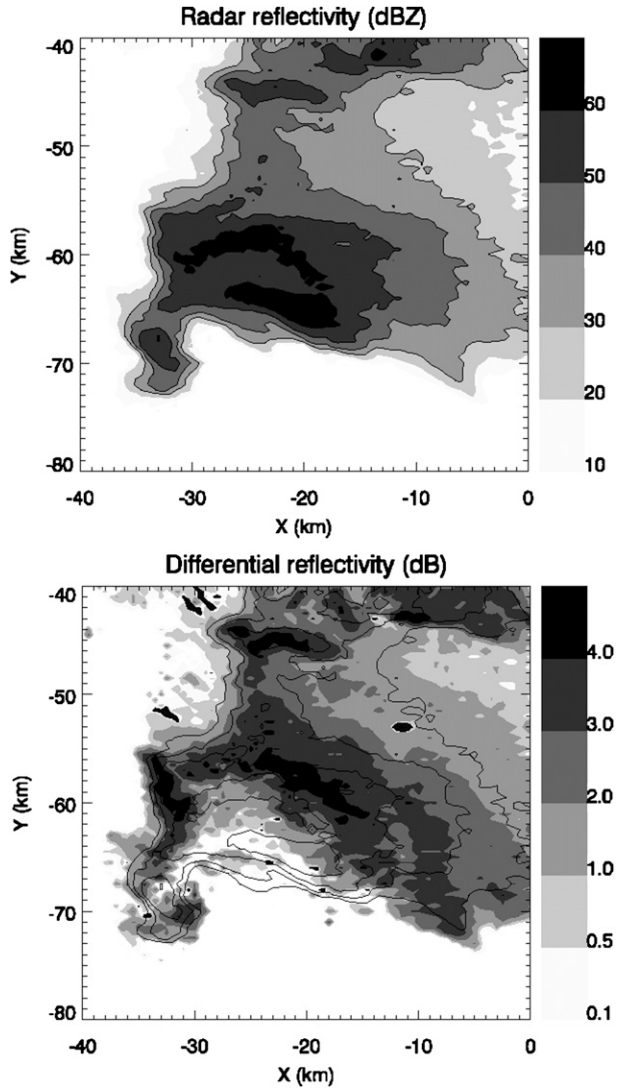

FIG. 12. Observed Z_{HH} and Z_{DR} hail signature from 0009 UTC 11 Apr 2007 from 0.5° elevation. The hail signature is disrupting the Z_{DR} arc signature in the Z_{DR} field, along the southern flank of the storm. Enhanced Z_{DR} at the periphery of the hail signature is due to a mixture of large drops resulting from melting hail and wet hailstones (which are sensed as giant raindrops).

echoes to ''split'' into left-moving and right-moving members in which the storm motion for each member deviates from the mean tropospheric wind. In instances of such storm splitting, the size sorting hypothesis predicts that an enhancement should be found on the north flank (inflow side) of the left split. In these cases, the left-moving storm motion vector can be found on the opposite side of the hodograph from the right moving member, such that the storm-relative winds have a northerly component and back with height (Fig. 13). The hodograph in Fig. 13 has been modified from the observed 20 May 2003 KOUN sounding from 0000 UTC. The observed sounding was taken approximately 1 h after a cold front passage and thus was not representative of the environment in which the supercells formed. The KOUN surface wind just before the cold front arrival was used instead, and the lowest-level wind observations that were contaminated by the front were omitted. The hodograph is used for illustrative purposes only; because of these subjective modifications, no quantitative calculations were performed.

The expected size sorting would result in an enhancement of Z_{DR} on the north side of the storm. The storm-relative hodograph indicates negative SRH, and we anticipate an analogous relation between negative SRH and the strength of the Z_{DR} arc. In fact, a Z_{DR} arc is observed on the north flank of the anticyclonic storm (Fig. 14). This has been seen in data from 8 May 2003, 19 May 2003, 24 May 2004, 10–11 April 2005, and 10–11 April 2007. We speculate that a left mover with a strong Z_{DR} arc, which indicates a substantial amount of negative SRH, may be long-lived and more conducive to large hail formation because of the sustenance of the mesoanticyclone. Lilly (1986) showed for idealized conditions that supercells may promote their own longevity. According to Lilly, the flow within supercell updrafts is characterized by high helicity, which may inhibit turbulent energy dissipation. For purely helical (Beltrami) flow, this turbulent energy cascade is

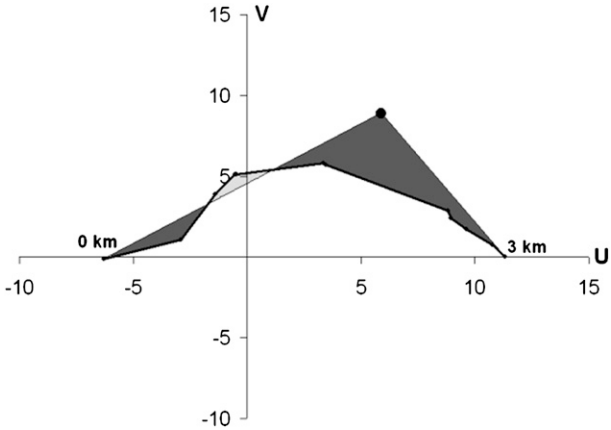

FIG. 13. Modified hodograph from 0000 UTC 20 May 2003 from KOUN. The original sounding from this time was approximately 1 h after a cold front passage; thus, the low-level winds were not representative of the environment in which the supercells developed. The surface wind from just before the cold front passage was used instead and the low-level observations contaminated by the front were omitted. The black dot represents the observed storm motion of the left mover. The dark (light) shading is proportional to the negative (positive) SRH. The u and v wind components are in m s^{-1}.

completely blocked. By analogy, a strong mesoanticyclone in a left mover may promote the storm's longevity.

b. Developing supercell and nonsupercell storms

The Z_{DR} arc is a signature intrinsic to supercell storms, but it can be useful in diagnosing nonsupercell storms that are transitioning into a supercellular mode or for identifying nonsupercell severe storms that take on supercell characteristics. On 8 May 2003 the Z_{DR} arc was observed for the first time in one of the storms as it began to transition into a supercell; this storm later went on to produce a damaging F-4 tornado in the Oklahoma City area (Romine et al. 2008). In at least three storms analyzed for this study (8 May 2003; 10 November 2004; 23 April 2008), the Z_{DR} arc appears before the development of the hook echo. Off-hodograph propagation of storms or storms that develop in helical environments should encounter wind shear conducive to the appearance of the Z_{DR} arc prior to the development of strong low-level rotation and the hook echo.

The signature has been observed in a few nonsupercell storms that went on to produce tornadoes (19 August 2005 near King City, Canada; 9 May 2007 in El Reno, Oklahoma; 15 November 2006 in southeastern Alabama). Data from these events are presented in Kumjian and Ryzhkov (2007, 2008), and Schenkman et al. (2008a,b) investigated the evolution of the El Reno event in detail. In each case, a particular cell embedded within a larger mesoscale convective system developed a Z_{DR} arc, indicating locally enhanced shear and SRH. This could be due to local variations in the environmental winds or some change in motion of the particular storm cell such that the storm-relative flow is enhanced. The cells that developed the signature produced the most significant reported severe weather in the mesoscale convective system.

5. Discussion and conclusions

It is documented that supercells can alter their nearby environment, especially the low-level winds (e.g., Browning 1964; Bluestein et al. 1988; Dowell and Bluestein 1997). Using observations from an instrumented tower, Dowell

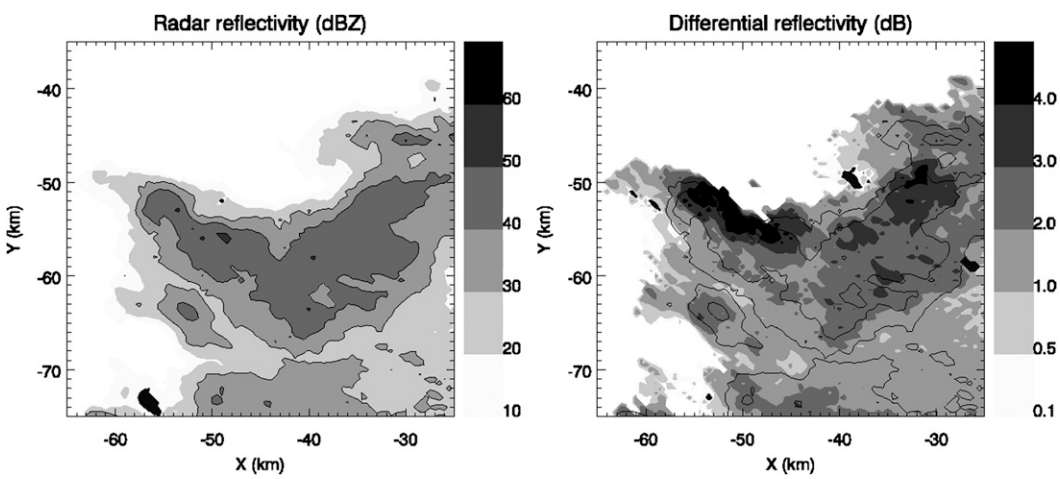

FIG. 14. Observed Z_{HH} and Z_{DR} for a left mover at 2303 UTC 19 May 2003 from the 0.0° elevation scan. A Z_{DR} arc is present on the north inflow flank of the storm, with Z_{DR} values in excess of 4 dB.

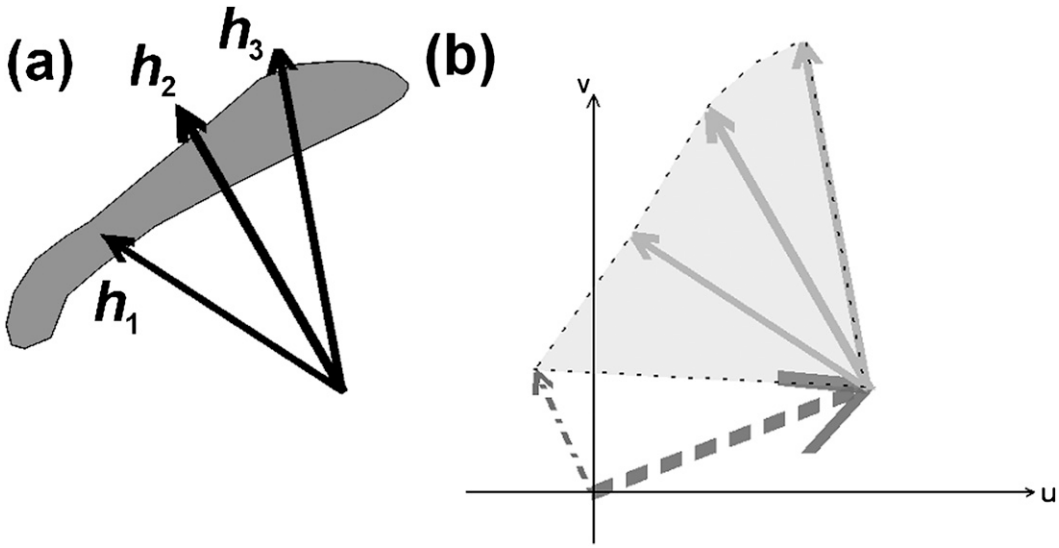

FIG. 15. Conceptual schematic explaining the relation between the Z_{DR} arc and the low-level SRH. In (a) the gray shaded region represents the Z_{DR} arc. The three black arrows are estimates of the storm-relative winds in the layer just above the Z_{DR} arc signature (generally the layer from about 1–3 km). (b) The local storm-relative wind estimates are plotted on a hodograph with the observed storm motion vector (large gray dashed vector); then the nearest surface wind report is plotted (small gray dashed–dotted vector). The low-level SRH is proportional to the light gray shaded area. No values are displayed on the hodograph because this is a qualitative assessment.

and Bluestein (1997) show strong vertical wind shear in the lowest 500 m that increased as a supercell approached. Their measurements from the edge of the FFD where the Z_{DR} arc is normally found indicated shear on the order of 0.01 s^{-1}. Such measurements of strong low-level shear have also been made by mobile Doppler radars (e.g., Bluestein and Pazmany 2000). Because the storms can influence their environments, the low-level shear and SRH could be potentially enhanced because of strong inflow. Because synoptic observations rarely sample the environment very near the storm, and because of the aforementioned significant variability in SRH, it is imperative for forecasters to assess any changes in the local environment due to the storm itself. The Z_{DR} arc may be a way to estimate local enhancements of shear and SRH.

From the alignment of the Z_{DR} arc, one can roughly approximate the mean storm-relative wind direction of the 1–2-km layer just above the observed signature, which should be more or less perpendicular to the major axis of the Z_{DR} arc. In a qualitative sense, the wind speed can be inferred as well (stronger winds cause more size sorting and thus a greater enhancement of Z_{DR}). By using this information in addition to the storm motion and surface wind speed, one can piece together a conceptual schematic of how the low-level hodograph, and thus SRH, is related to the Z_{DR} arc signature (Fig. 15). This conceptual framework could be used to make a qualitative estimate of the SRH at low levels. The storm motion can be estimated by tracking radar echoes from previous volume scans. Observations of the surface wind from stations near the storm inflow environment should be used to estimate the surface wind vector. Thus, the low-level SRH can be roughly estimated by combining the surface wind vector, storm motion vector, and estimated storm-relative winds in the layer immediately above the Z_{DR} arc. This method is similar to the one advocated in Davies-Jones et al. (1990) and may be particularly useful in situations in which the radiosonde observations are spatially and/or temporally unrepresentative of the storm inflow environment.

The results from this paper indicate that a positive relation exists between the magnitude of the Z_{DR} values in the arc signature and the low-level SRH. Increasing wind shear will increase the amount of size sorting that occurs, which subsequently manifests itself as an increase in Z_{DR}. Because SRH takes wind shear into account with other factors, generally there should be a positive relation for supercells or storms with motion off the hodograph. Obviously one can envision situations of large shear but low SRH in which the relation may not hold, so the relation is not perfect. Nonetheless, the relation between a radar observation and strong wind shear (and subsequently SRH) is potentially important, especially when the measurement

is made at the storm location. We are not claiming that all Z_{DR} enhancements are related to SRH; in fact, the Z_{DR} arc signature appears to be unique in that such a relation evidently exists.

In summary,

1) Size sorting due to speed and directional wind shear, which can be augmented by low-level inflow, results in an enhancement of Z_{DR} along the edge of the storm's FFD precipitation echo, generally along a gradient in Z_{HH}. The location, shape, shallowness, and alignment of this signature, called the Z_{DR} arc, are distinct among other size-sorting induced enhancements of Z_{DR}.
2) Increased storm-relative wind speed and directional shear tend to increase the area swept out by the hodograph, enhancing the SRH. As low-level SRH values increase, the size sorting due to the enhanced storm-relative wind shear generally increases. This results in larger Z_{DR} values in the arc signature. The conceptual model presented here suggests a positive relation between low-level SRH values and the magnitude of the Z_{DR} in the signature. Idealized numerical simulations have verified this positive relation, and observational evidence supporting the conceptual model is discussed.
3) In both tornadic and nontornadic supercells, the Z_{DR} arc tends to extend to the updraft region in times leading up to the occlusion of the low-level mesocyclone. Once the occlusion takes place, the Z_{DR} arc appears to be disrupted by a hail signature. There is some indication that in nontornadic supercells the Z_{DR} arc signature is disrupted more persistently, possibly indicating that outflow from the FFD is interfering with processes necessary for tornadogenesis.
4) Because the Z_{DR} arc is measured within the storm, it characterizes the immediate inflow environment well and could potentially be employed to refine estimates of low-level SRH.

Acknowledgments. This work evolved from part of an M.S. thesis at the University of Oklahoma and is supported under NSF Grant ATM-0532107. Additional funding was provided by NOAA/Office of Oceanic and Atmospheric Research under NOAA–University of Oklahoma Cooperative Agreement NA17RJ1227, U.S. Department of Commerce. The authors thank the NSSL/CIMMS scientists and engineers who maintain and operate the KOUN polarimetric radar and signal processing software for research-grade applications. We also acknowledge useful discussions with Scott Giangrande. Robert Davies-Jones, Dušan Zrnić, and Evgeni Fedorovich reviewed earlier versions of the manuscript and provided very useful comments and suggestions that improved the paper. Additionally, comments from an anonymous reviewer helped clarify aspects of our work.

REFERENCES

Atlas, D., and C. W. Ulbrich, 1977: Path- and area-integrated rainfall measurement by microwave attenuation in the 1–3-cm band. *J. Appl. Meteor.,* **16,** 1322–1331.

——, R. C. Srivastava, and R. S. Sekhon, 1973: Doppler radar characteristics of precipitation at vertical incidence. *Rev. Geophys.,* **11,** 1–35.

Beard, K. V., 1976: Terminal velocity and shape of cloud and precipitation drops aloft. *J. Atmos. Sci.,* **33,** 851–864.

Bluestein, H. B., and A. L. Pazmany, 2000: Observations of tornadoes and other convective phenomena with a mobile, 3-mm wavelength Doppler radar: The spring 1999 field experiment. *Bull. Amer. Meteor. Soc.,* **81,** 2939–2951.

——, E. W. McCaul Jr., G. P. Byrd, and G. R. Woodall, 1988: Mobile sounding observations of a tornadic storm near the dryline: The Canadian, Texas storm of 7 May 1986. *Mon. Wea. Rev.,* **116,** 1790–1804.

——, M. M. French, R. L. Tanamachi, S. Frasier, K. Hardwick, F. Junyent, and A. Pazmany, 2007: Close-range observations of tornadoes in supercells made with a dual-polarization, X-band, mobile Doppler radar. *Mon. Wea. Rev.,* **135,** 1522–1543.

Brandes, E. A., and K. Ikeda, 2004: Freezing-level estimation with polarimetric radar. *J. Appl. Meteor.,* **43,** 1541–1553.

——, J. Vivekanandan, J. D. Tuttle, and C. J. Kessinger, 1995: A study of thunderstorm microphysics with multiparameter radar and aircraft observations. *Mon. Wea. Rev.,* **123,** 3129–3143.

——, ——, and ——, 2004: Drop size distribution retrieval with polarimetric radar: Model and application. *J. Appl. Meteor.,* **43,** 461–475.

Bringi, V. N., and V. Chandrasekar, 2001: *Polarimetric Doppler Weather Radar*. Cambridge University Press, 336 pp.

——, ——, J. Hubbert, E. Gorgucci, W. Randeu, and M. Schoenhuber, 2003: Raindrop size distribution in different climatic regimes from disdrometer and dual-polarized radar analysis. *J. Atmos. Sci.,* **60,** 354–365.

Brooks, H. E., C. A. Doswell III, and R. P. Davies-Jones, 1993: Environmental helicity and the maintenance and evolution of low-level mesocyclones. *The Tornado: Its Structure, Dynamics, Prediction, and Hazards, Geophys. Monogr.,* Vol. 79, Amer. Geophys. Union, 97–104.

Browning, K. A., 1964: Airflow and precipitation trajectories within severe local storms which travel to the right of the winds. *J. Atmos. Sci.,* **21,** 634–639.

——, 1965: The evolution of tornadic storms. *J. Atmos. Sci.,* **22,** 664–668.

——, and R. J. Donaldson Jr., 1963: Airflow and structure of a tornadic storm. *J. Atmos. Sci.,* **20,** 533–545.

Cao, Q., G. Zhang, E. Brandes, T. Schuur, A. V. Ryzhkov, and K. Ikeda, 2008: Analysis of video disdrometer and polarimetric radar data to characterize rain microphysics in Oklahoma. *J. Appl. Meteor. Climatol.,* **47,** 2238–2255.

Caylor, I., and A. J. Illingworth, 1987: Radar observations and modeling of warm rain initiation. *Quart. J. Roy. Meteor. Soc.,* **113,** 1171–1191.

Colquhoun, J. R., and P. A. Riley, 1996: Relationships between tornado intensity and various wind and thermodynamic variables. *Wea. Forecasting,* **11,** 360–371.

Conway, J. W., and D. S. Zrnić, 1993: A study of embryo production and hail growth using dual-Doppler and multiparameter radars. *Mon. Wea. Rev.,* **121,** 2511–2528.

Davies, J. M., and R. H. Johns, 1993: Some wind and instability parameters associated with strong and violent tornadoes. Part I: Wind shear and helicity. *The Tornado: Its Structure, Dynamics, Prediction, and Hazards, Geophys. Monogr.*, Vol. 79, Amer. Geophys. Union, 573–582.

Davies-Jones, R., 1984: Streamwise vorticity: The origin of updraft rotation in supercell thunderstorms. *J. Atmos. Sci.,* **41,** 2991–3006.

——, 1993: Helicity trends in tornado outbreaks. Preprints, *17th Conf. on Severe Local Storms*, St. Louis, MO, Amer. Meteor. Soc., 56–60.

——, 2008: Can a descending rain curtain in a supercell instigate tornadogenesis barotropically? *J. Atmos. Sci.,* **65,** 2469–2497.

——, D. W. Burgess, and M. Foster, 1990: Test of helicity as a forecast parameter. Preprints, *16th Conf. on Severe Local Storms*, Kananaskis Park, AB, Canada, Amer. Meteor. Soc., 588–592.

Dowell, D. C., and H. B. Bluestein, 1997: The Arcadia, Oklahoma storm of 17 May 1981: Analysis of a supercell during tornadogenesis. *Mon. Wea. Rev.,* **125,** 2562–2582.

——, C. R. Alexander, J. M. Wurman, and L. J. Wicker, 2005: Centrifuging of hydrometeors and debris in tornadoes: Radar reflectivity patterns and wind-measurement errors. *Mon. Wea. Rev.,* **133,** 1501–1524.

Droegemeier, K. K., S. M. Lazarus, and R. P. Davies-Jones, 1993: The influence of helicity on numerically simulated convective storms. *Mon. Wea. Rev.,* **121,** 2005–2029.

Esterheld, J. M., and D. J. Giuliano, 2008: Discriminating between tornadic and non-tornadic supercells: A new hodograph technique. *Electron. J. Severe Storms Meteor.,* **3,** 1–50.

Giangrande, S. E., A. V. Ryzhkov, and J. Krause, 2005: Automatic detection of the melting layer with a polarimetric prototype of the WSR-88D radar. Preprints, *32nd Int. Conf. on Radar Meteorology*, Albuquerque, NM, Amer. Meteor. Soc., 11R.2. [Available online at http://ams.confex.com/ams/pdfpapers/95894.pdf.]

——, J. M. Krause, and A. V. Ryzhkov, 2008: Automatic designation of the melting layer with a polarimetric prototype of the WSR-88D radar. *J. Appl. Meteor. Climatol.,* **47,** 1354–1364.

Goddard, J. W. F., S. M. Cherry, and V. N. Bringi, 1982: Comparison of dual-polarization radar measurements of rain with ground-based disdrometer measurements. *J. Appl. Meteor.,* **21,** 252–256.

Gunn, R., and G. D. Kinzer, 1949: The terminal velocity of fall for water droplets in stagnant air. *J. Meteor.,* **6,** 243–248.

——, and J. S. Marshall, 1955: The effect of wind shear on falling precipitation. *J. Meteor.,* **12,** 339–349.

Herzegh, P. H., and A. R. Jameson, 1992: Observing precipitation through dual-polarization radar measurements. *Bull. Amer. Meteor. Soc.,* **73,** 1365–1374.

Hitschfeld, W., 1960: The motion and erosion of convective storms in severe vertical wind shear. *J. Atmos. Sci.,* **17,** 270–282.

Höller, H., V. N. Bringi, J. Hubbert, M. Hagen, and P. F. Meischner, 1994: Life cycle and precipitation formation in a hybrid-type hailstorm revealed by polarimetric and Doppler radar measurements. *J. Atmos. Sci.,* **51,** 2500–2522.

Hubbert, J., V. N. Bringi, L. D. Carey, and S. Bolen, 1998: CSU-CHILL polarimetric measurements from a severe hailstorm in eastern Colorado. *J. Appl. Meteor.,* **37,** 749–755.

Illingworth, A. J., J. W. F. Goddard, and S. M. Cherry, 1987: Polarization radar studies of precipitation development in convective storms. *Quart. J. Roy. Meteor. Soc.,* **113,** 469–489.

Jameson, A. R., and D. B. Johnson, 1983: Cloud microphysics and radar. *Radar in Meteorology: Battan Memorial and 40th Anniversary Radar Meteorology Conference*, Amer. Meteor. Soc., 323–340.

Kennedy, P. C., S. A. Rutledge, W. A. Petersen, and V. N. Bringi, 2001: Polarimetric radar observations of hail formation. *J. Appl. Meteor.,* **40,** 1347–1366.

Kerr, B. W., and G. L. Darkow, 1996: Storm-relative winds and helicity in the tornadic thunderstorm environment. *Wea. Forecasting,* **11,** 489–505.

Klemp, J. B., 1987: The dynamics of tornadic thunderstorms. *Annu. Rev. Fluid Mech.,* **19,** 369–402.

——, and R. B. Wilhelmson, 1978: Simulations of right- and left-moving storms produced through storm splitting. *J. Atmos. Sci.,* **35,** 1097–1110.

——, and R. Rotunno, 1983: A study of the tornadic region within a supercell thunderstorm. *J. Atmos. Sci.,* **40,** 359–377.

Kumjian, M. R., and A. V. Ryzhkov, 2007: Polarimetric characteristics of tornadic and nontornadic supercell thunderstorms. Preprints, *33rd Conf. on Radar Meteorology,* Cairns, Queensland, Australia, Amer. Meteor. Soc., P10.1. [Available online at http://ams.confex.com/ams/pdfpapers/122882.pdf.]

——, and ——, 2008: Polarimetric signatures in supercell thunderstorms. *J. Appl. Meteor. Climatol.,* **47,** 1940–1961.

——, ——, J. L. Alford, M. Knight, and J. W. Conway, 2008: Close-range observations of a tornadic supercell with C-band polarimetric Doppler radar. Preprints, *Symp. on Recent Developments in Atmospheric Applications of Radar and Lidar,* New Orleans, LA, Amer., Meteor. Soc., P2.14. [Available online at http://ams.confex.com/ams/pdfpapers/133441.pdf.]

Leftwich, P. W., 1990: On the use of helicity in operational assessment of severe local storm potential. Preprints, *16th Conf. on Severe Local Storms,* Kananaskis Park, AB, Canada, Amer. Meteor. Soc., 269–274.

Lemon, L. R., and C. A. Doswell, 1979: Severe thunderstrom evolution and mesocyclone structure as related to tornadogenesis. *Mon. Wea. Rev.,* **107,** 1184–1197.

Lilly, D. K., 1986: The structure, energetics, and propagation of rotating convective storms. Part II: Helicity and storm stabilization. *J. Atmos. Sci.,* **43,** 126–140.

Loney, M. L., D. S. Zrnić, J. M. Straka, and A. V. Ryzhkov, 2002: Enhanced polarimetric radar signatures above the melting layer in a supercell storm. *J. Appl. Meteor.,* **41,** 1179–1194.

Maddox, R. A., 1976: An evaluation of tornado proximity wind and stability data. *Mon. Wea. Rev.,* **104,** 133–142.

Markowski, P. M., 2002: Hook echoes and rear-flank downdrafts: A review. *Mon. Wea. Rev.,* **130,** 852–876.

——, J. M. Straka, E. N. Rasmussen, and D. O. Blanchard, 1998: Variability of storm-relative helicity during VORTEX. *Mon. Wea. Rev.,* **126,** 2959–2971.

——, ——, and ——, 2002: Direct surface thermodynamic observations within the rear-flank downdrafts of nontornadic and tornadic supercells. *Mon. Wea. Rev.,* **130,** 1692–1721.

——, ——, and ——, 2003: Tornadogenesis resulting from the transport of circulation by a downdraft: Idealized numerical simulations. *J. Atmos. Sci.,* **60,** 795–823.

Meischner, P. F., V. N. Bringi, D. Heimann, and H. Höller, 1991: A squall line in Southern Germany: Kinematics and precipitation formation as deduced by advanced polarimetric and Doppler radar measurements. *Mon. Wea. Rev.,* **119,** 678–701.

Mishchenko, M. I., 2000: Calculation of the amplitude matrix for a nonspherical particle in a fixed orientation. *Appl. Opt.,* **39,** 1026–1031.

Outinen, K., and J. Teittinen, 2007: Case study of a tornadic supercell in Finland 28 August 2005. *Proc. Fourth European Conf. on Severe Storms,* Trieste, Italy, International Centre for Theoretical Physics, 05.14.

——, and ——, 2008: Polarimetric radar observations of a tornadic supercell in Finland. *Proc. Fifth European Conf. on Radar in Meteorology and Hydrology*, Helsinki, Finland, Finnish Meteorological Institute, P4.3.

Pruppacher, H. R., and R. L. Pitter, 1971: A semi-empirical determination of the shape of cloud and rain drops. *J. Atmos. Sci.,* **28,** 86–94.

Rasmussen, E. N., and D. O. Blanchard, 1998: A baseline climatology of sounding-derived supercell and tornado forecast parameters. *Wea. Forecasting,* **13,** 1146–1164.

Richardson, Y. P., K. K. Droegemeier, and R. P. Davies-Jones, 2007: The influence of horizontal environmental variability on numerically simulated convective storms. Part I: Variations in vertical shear. *Mon. Wea. Rev.,* **135,** 3429–3455.

Romine, G. S., D. W. Burgess, and R. B. Wilhelmson, 2008: A dual-polarization-radar-based assessment of the 8 May 2003 Oklahoma City area tornadic supercell. *Mon. Wea. Rev.,* **136,** 2849–2870.

Rotunno, R., and J. B. Klemp, 1982: The influence of the shear-induced pressure gradient on thunderstorm motion. *Mon. Wea. Rev.,* **110,** 136–151.

——, and ——, 1985: On the rotation and propagation of simulated supercell thunderstorms. *J. Atmos. Sci.,* **42,** 271–292.

Ryzhkov, A. V., and D. S. Zrnić, 1998: Discrimination between rain and snow with a polarimetric radar. *J. Appl. Meteor.,* **37,** 1228–1240.

——, T. J. Schuur, D. W. Burgess, and D. S. Zrnić, 2005: Polarimetric tornado detection. *J. Appl. Meteor.,* **44,** 557–570.

Sachidananda, M., and D. S. Zrnić, 1987: Rain rate estimated from differential polarization measurements. *J. Atmos. Oceanic Technol.,* **4,** 588–598.

Schenkman, A. D., A. M. Shapiro, K. Brewster, M. Xue, J. Gao, and N. Snook, 2008a: High-resolution assimilation of CASA radar data from a tornadic convective system. Preprints, *Symp. on Recent Developments in Atmospheric Applications of Radar and Lidar,* New Orleans, LA, Amer. Meteor. Soc., P1.6. [Available online at http://ams.confex.com/ams/pdfpapers/132040.pdf.]

——, C. M. Shafer, and M. R. Kumjian, 2008b: Multi-platform analysis of a tornadic convective system. *Proc. Fifth European Conf. on Radar in Meteorology and Hydrology*, Helsinki, Finland, Finnish Meteorological Institute, P4.10.

Schuur, T. J., A. V. Ryzhkov, D. S. Zrnić, and M. Schönhuber, 2001: Drop size distributions measured by a 2D video disdrometer: Comparison with dual-polarization radar data. *J. Appl. Meteor.,* **40,** 1019–1034.

Seliga, T. A., and V. N. Bringi, 1976: Potential use of radar differential reflectivity measurements at orthogonal polarizations for measuring precipitation. *J. Appl. Meteor.,* **15,** 69–76.

Snyder, J. C., 2008: Attenuation correction techniques and hydrometeor classification of high-resolution, X-band, dual-polarized mobile radar data of severe convective storms. M.S. thesis, School of Meteorology, University of Oklahoma, 148 pp.

Thompson, R. L., and R. Edwards, 2000: An overview of environmental conditions and forecast implications of the 3 May 1999 tornado outbreak. *Wea. Forecasting,* **15,** 682–699.

——, ——, J. A. Hart, K. L. Elmore, and P. Markowski, 2003: Close proximity soundings within supercell environments obtained from the Rapid Update Cycle. *Wea. Forecasting,* **18,** 1243–1261.

——, C. M. Mead, and R. Edwards, 2007: Effective storm-relative helicity and bulk shear in supercell thunderstorm environments. *Wea. Forecasting,* **22,** 102–115.

Tuttle, J. D., V. N. Bringi, H. D. Orville, and F. J. Kopp, 1989: Multiparameter radar study of a microburst: Comparison with model results. *J. Atmos. Sci.,* **46,** 601–620.

Ulbrich, C. W., 1983: Natural variations in the analytical form of the raindrop size distribution. *J. Climate Appl. Meteor.,* **22,** 1764–1775.

Van Den Broeke, M. S., J. M. Straka, and E. N. Rasmussen, 2008: Polarimetric radar observations at low levels during tornado life cycles in a small sample of classic Southern Plains supercells. *J. Appl. Meteor. Climatol.,* **47,** 1232–1247.

Wakimoto, R. M., and V. N. Bringi, 1988: Dual-polarization observations of microbursts associated with intense convection: The 20 July storm during the MIST project. *Mon. Wea. Rev.,* **116,** 1521–1539.

Weisman, M. L., and J. B. Klemp, 1984: The structure and classification of numerically simulated convective storms in directionally varying wind shears. *Mon. Wea. Rev.,* **112,** 2479–2498.

——, and R. Rotunno, 2000: The use of vertical wind shear versus helicity in interpreting supercell dynamics. *J. Atmos. Sci.,* **57,** 1452–1472.

Wicker, L. J., and R. B. Wilhelmson, 1995: Simulation and analysis of tornado development and decay within a three-dimensional supercell thunderstorm. *J. Atmos. Sci.,* **52,** 2675–2703.

Yu, T.-Y., R. R. Rondinel, and R. D. Palmer, 2009: Investigation of non-Gaussian weather spectra observed by weather radar in a tornadic supercell. *J. Atmos. Oceanic Technol.,* in press.

Zrnić, D. S., and A. V. Ryzhkov, 1999: Polarimetry for weather surveillance radars. *Bull. Amer. Meteor. Soc.,* **80,** 389–406.